Journal of Innovative Optical Health Sciences
Vol. 2, No. 2 (2009) 149–163


World Scientific
www.worldscientific.com



# RADIATIVE TRANSPORT IN THE DELTA-P1 APPROXIMATION FOR LAMINAR OPTICAL TOMOGRAPHY

BAOHONG YUAN
*Department of Biomedical Engineering*
*Catholic University of America*
*Washington DC 20064, USA*
*yuan@cua.edu*

To provide a computational efficient forward model with moderate accuracy for rapid 3D optical tomography in small volumes, radiative transport in the delta-P1 approximation combined with the approximation of the reciprocity was examined. Perturbations of optical signals caused by absorption and fluorescence heterogeneities submerged in a resin-based liquid phantom with background parameters close to rat brain tissues were measured using a recently constructed laminar optical tomography system. These measured perturbations were used to examine the theoretically calculated fluence perturbations based on the delta-P1 approximation and the reciprocity approximation. Results show that the errors between the predicted and measured data are acceptable, especially for fluorescence perturbations.

*Keywords*: Photon migration; tomography; fluorescence; delta-P1 approximation; reciprocity approximation.

## 1. Introduction

Optical absorption or fluorescent contrast generated by tissue chromophores or fluorophores, such as hemoglobin, melanin, and endogenous/exogenous fluorescent dyes, provides unique tissue functional information.[1−9] Over the past years, various optical techniques have been developed for 3-dimensional (3D) and functional imaging in living tissue, such as optical microscopy,[2] spectroscopy[3,4] and (fluorescence) diffuse optical tomography (DOT).[5−9] These promising techniques have been intensively investigated for disease detection, diagnosis, and treatment monitoring.[2−9] Recently, 3D optical imaging in mesoscopic volumes is attracting considerable interests due to numerous potential applications to small animal imaging and superficial tissue imaging.[10−18] As an example, laminar optical tomography (LOT) was proposed and developed for functionally imaging stratified tissue, such as homodynamic response and neurovascular coupling in rat cortex,[14] transmural propagation of electrical waves in rat heart,[15] and human skin lesion boundaries.[18] LOT is a hybrid technique that combines the instrumentation of laser scanning confocal microscopy, with the imaging approach of diffuse optical tomography.[13−18] By measuring multiple-scattered light over distances of only a few millimeters between source-detector pairs, LOT can maintain high levels of resolution ($< 200$ microns), which is much higher than DOT, and yet LOT can probe tissues beyond the scattering limit encountered by microscopy (2–3 mm depth).[13−18]

Rapid image reconstruction is highly desirable in many applications, such as homodynamic response to external stimuli and neurovascular coupling in rat cortex.[14] A recently developed LOT system can reach a data-acquisition speed as high as 100 frames/s, which eliminates hardware

limitations for applications of rapid imaging.[16,17] Since the imaging volume in LOT is usually much smaller than that in conventional DOT,[13−18] Monte Carlo (MC) simulation, a computational intensive model, was adopted previously for calculating signal perturbations caused by optical heterogeneities, because the standard photon diffuse approximation (SDA) used in DOT is invalid.[10−12] Consequently, the speed of image reconstruction in LOT is mainly limited due to the intensive computations of MC simulations. On the other hand, it is well known that analytical models, such as diffusion approximations, can provide efficient calculations for fluence perturbations (but suffers from low accuracy in small volumes).[10−12] Radiative transport in the delta-P1 approximation, as an improved diffusion approximation, has been developed and validated that it maintains considerably high accuracy for estimating surface diffuse reflectance even when source–detector separation is reduced to as short as one fifth of one transport mean free path.[19−24] However, the applicability of delta-P1 approximation to 3D tomographical imaging has not been validated. To provide a computational efficient model for rapid LOT imaging, delta-P1 approximation is evaluated in this study by comparing the theoretically calculated fluence perturbations (including absorption and fluorescence perturbations) with the experimentally measured perturbations in phantoms. Results show that the errors between the predicted and measured data are acceptable, especially for fluorescence perturbations.

This paper is organized as follows: the delta-P1 is briefly introduced in Sec. 2, and the materials, system, and experiments are presented in Sec. 3. Results and discussions are detailed in Sec. 4 and conclusions are given in Sec. 5.

## 2. Forward Models

### 2.1. *Delta-P1 approximation*

By introducing a delta function to the single scattering phase function to better accommodate the strong forward scattering of tissue, and considering a collimated light source that "generates" the diffuse light, Star[1,19] and Prahl[20] first proposed delta-P1 approximation to improve the prediction accuracy of diffuse reflectance relative to standard diffuse approximation for one-dimensional geometry media. Venugopalan *et al.* further developed and quantified the delta-P1 theory for a 3D medium.[21−24] A brief introduction to delta-P1 approximation is given below, specifically for a collimated laser beam launched normally to a semi-infinite medium. The governing equations of fluence in the delta-P1 approximation are given as follows[21−22]:

$$\nabla^2\Phi_d(r) - \mu_{\text{eff}}^2\Phi_d(r) = -3\mu_s^*(\mu_{tr} + \mu_t^* g^*)\Phi_c(z)\delta(1 - \hat{r}\cdot\hat{z}), \quad (1)$$

$$\Phi_c(z) = P_0(1 - R_s)\exp(-\mu_t^* z), \quad (2)$$

$$\Phi_{\text{total}}(r) = \Phi_d(r) + \Phi_c(z)\delta(1 - \hat{r}\cdot\hat{z})), \quad (3)$$

where $\Phi_d$ is diffused fluence, $\Phi_c$ collimated fluence, $\mu_{\text{eff}} = \sqrt{3\mu_a\mu_{tr}}$, $\mu_{tr} = \mu_a + \mu_s'$, $g^* = g/(1+g)$, $\mu_s^* = \mu_s'(1+g)$, $\mu_t^* = \mu_a + \mu_s^*$, $\mu_a$ absorption coefficient, $\mu_s$ scattering coefficient, $g$ anisotropy factor, $P_0$ laser power, and $R_s$ the reflection coefficient at tissue–air boundary, respectively. Combining Eqs. (1)–(3) with an extrapolated boundary condition for a semi-infinite medium,[25] the diffused fluence $\Phi_d$ can be solved as

$$\Phi_d(\rho, z) = \frac{A}{4\pi D}\int_0^\infty \left[\frac{\exp(-\mu_{\text{eff}} r_1)}{r_1} - \frac{\exp(-\mu_{\text{eff}} r_2)}{r_2}\right]\exp(-\mu_t^* z')dz', \quad (4)$$

where $A = (\mu_t^* + \mu_a g^*)\mu_s^*/\mu_{tr}$, $D = 1/(3\mu_{tr})$ (diffusion coefficient), $r_1 = [\rho^2 + (z - z')^2]^{1/2}$, $r_2 = [\rho^2 + (z + z' + 2z_b)^2]^{1/2}$, $\rho^2 = x^2 + y^2$, $z'$ is the position of any point on the line source, $z_b = 2D(1 + R_1)/(1 - R_1)$, and $R_1$ is the effective Fresnel reflection coefficient for unpolarized light. Figure 1 depicts the configuration of all geometrical parameters, and all the parameters in Eq. (4) have been defined in Refs. 21 and 22. Gaussian quadrature with a Legendre polynomial weighting function was adopted to calculate the line integration and the diffused fluence in Eq. (4).[22] The total fluence is given by Eq. (3).

### 2.2. *Fluence perturbations*

In 3D tomographic imaging, fluence perturbations caused by an absorbing or fluorescent heterogeneity at different locations ($x$, $y$ and $z$) are calculated based on a forward model for different source–detector pairs, and compared with the experimentally measured perturbations of the diffused reflectance. Therefore, the accuracies of the calculated fluence perturbations (mainly determined by the forward model) directly affect the accuracies of the reconstructed optical parameters. In DOT, when

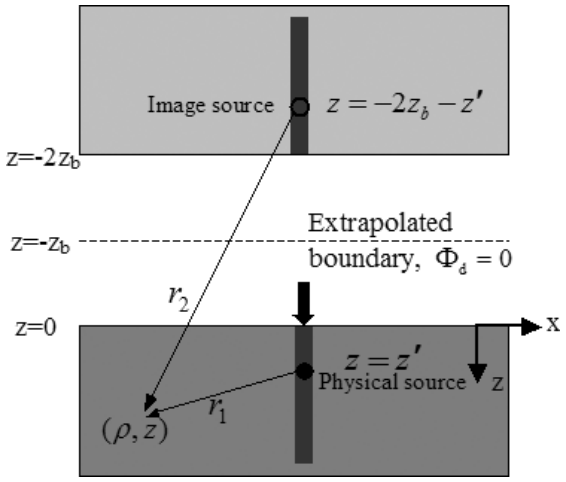


Fig. 1. Schematic drawing of the extrapolated boundary condition with a line source.

an analytical forward model is employed, Green's function of a point source is usually adopted to calculate the fluence perturbations.[4–9] For LOT the fluence perturbations were calculated based on an assumption of reciprocity in which the probability of a photon propagating from point A to point B is assumed equal to the probability of a photon propagating from point B to point A (see Appendix B for details).[13–15,26–28] Based on the assumption of the reciprocity, the relative perturbation of fluence for a source–detector pair can be expressed as:

$$\frac{\Delta\Phi_i}{\Phi_{0i}} = \sum_{j=1}^{N} W_{ij}(r_{si}, r_j, r_{di}) \left( \frac{\Phi_0(r_{si}, r_0)}{S_0} \Delta\mu_a(r_j) \right), \tag{5}$$

where $\Delta\Phi_i/\Phi_{0i} = (\Phi_i - \Phi_{0i})/\Phi_{0i}$ is the relative perturbation of fluence of the $i$th source–detector pair; $r_{si}$ and $r_{di}$ are the position of the $i$th source and detector, respectively; $r_j$ is the position of the $j$th voxel in the medium; $N$ is the total number of voxels in the imaging volume; $\Phi_0(r_{si}, r_0)$ is the fluence at position $r_0$ generated by the $i$th source at position $r_{si}$; $S_0$ is a power constant; and $\Delta\mu_a(r_j)$ is the perturbation of absorption coefficient at the $j$th voxel. The sensitivity matrix $W_{ij}(r_{si}, r_j, r_{di})$ is expressed as:

$$\begin{aligned} W_{ij}(r_{si}, r_j, r_{di}) &= -\Delta v \cdot \left( \frac{\Phi_0(r_{si}, r_j)}{\Phi_0(r_{si}, r_0)} \right) \\ &\quad \cdot \left( \frac{\Phi_0(r_{si}, |\mathbf{r}_j - \mathbf{r}_{di}|)}{\Phi_0(r_{si}, r_0)} \right) \Bigg/ \left( \frac{\Phi_0(r_{si}, r_{di})}{\Phi_0(r_{si}, r_0)} \right), \end{aligned} \tag{6}$$

where $\Delta v$ is the voxel volume, $\Phi_0(r_{si}, r_0)$ is the fluence at any position $r_0$ generated by the $i$th source at position $r_{si}$ and is used as a normalization factor that makes the sensitivity matrix nondimensional. The principle of reciprocity has been used in Eq. (6) (see Appendix B for details). Rytov approximation is used to connect experimentally measured signal perturbation and the theoretically calculated fluence perturbation by the following equation[5,6,29]:

$$\frac{\Delta M_i}{M_{0i}} \approx \exp\left( \frac{\Delta\Phi_i}{\Phi_{0i}} \right) - 1. \tag{7}$$

$M_{0i}$ is the measured signal of the $i$th source–detector pair without the perturbation of the optical parameter and $\Delta M_i = M_i - M_{0i}$ is the difference between the measured signals with and without the perturbation in the optical parameter.

In this study, fluence is assumed to be proportional to the experimentally measured signal. To examine the validity of this assumption in LOT, the following analysis is given. Based on Eq. (A1), the measured signal in LOT is proportional to the angular integration of the diffused reflectance at the medium surface within the acceptance angle of the LOT system. The angular distribution of the diffused reflectance at any point along radial direction was simulated using MC simulation,[30,31] and is integrated from $-4.5$ to 4.5 degrees (a typical acceptance angle in LOT[16,18] and zero degree represents the outward direction normal to the medium surface). The integrated value represents the measured LOT "signal" at the position. The signal is plotted as a function of the radial distance indicated by a dashed line in Fig. 2. On the other hand, the fluence (just underneath the medium surface) is also calculated from the same MC simulation, which is shown as a solid line. To examine the relationship between the signal and the fluence, the ratio of the fluence to the signal was plotted as a dotted line in Fig. 2. The dash-dot line almost represents a constant except in the region close to the source position. The black dotted line indicates the constant (for eye guide). When the radial distance $\rho$ is less than $\sim 0.33$ mm, the ratio diverges from the constant. The radial distance at which the ratio diverges from the constant is defined as starting-diverging-distance ($l$) and is indicated on Fig. 2. A finite width of a laser beam (50 microns in radius) in the MC simulation causes the jumps of the curves. This result implies that the LOT's signal is proportional to the fluence around the boundary except for very short source–detector separations.

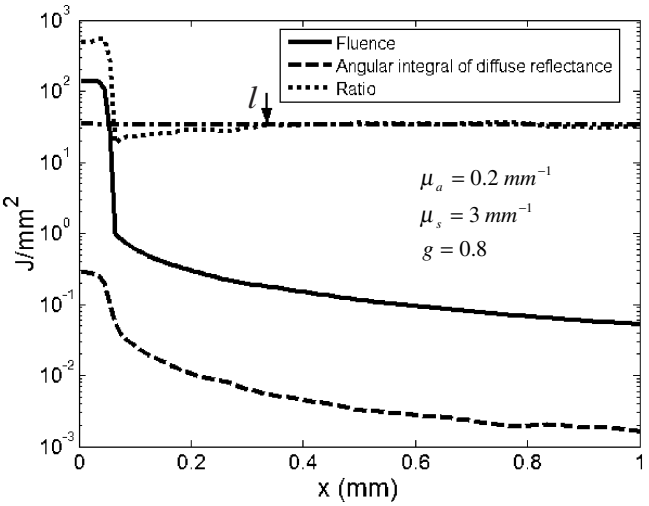


Fig. 2. MC simulation of fluence, angular integral of diffuse reflectance and ratio between them as a function of lateral distance $x$ from the light source. The source is assumed as a flat beam with a radius of 50 microns and total energy of 1 Joule.

Therefore, Eq. (4) can be used to calculate fluence distribution in a semi-infinite medium and Eq. (6) can be used to calculate the sensitivity matrix in terms of the calculated fluence from Eq. (4). Based on the sensitivity matrix and a given perturbation in absorption coefficient, Eq. (5) can be used to calculate the relative perturbation of the fluence. Eventually, Eq. (7) is used to predict the normalize signal perturbations in experiments. By comparing the perturbation calculated from Eq. (7) with the experimentally measured perturbation from the LOT system, one can analyze the accuracy of the delta-P1 approximation.

## 3. Materials, System, and Experiments

A resin-based liquid phantom was adopted in present study and the details can be found in Refs. 32 and 33. Briefly, epoxy resin was dissolved with certain amount of a dye and Tiranti opaque white polyester pigment to mimic a homogeneous tissue. The dye and the white polyester pigment were used to generate light absorption and scattering, respectively. After careful calibration, the absorption coefficient and the reduced scattering coefficient at 532 nm were $\mu_\alpha = 0.2\,\mathrm{mm}^{-1}$ and $\mu_s' = 0.6\,\mathrm{mm}^{-1}$, respectively, which are typical values of rat's brain tissue.[14] The refractive index is 1.58 based on Ref. 32. An absorbing stick ($\sim 500$ microns diameter) was used to mimic absorption perturbations. The absorption coefficient and the reduced scattering coefficient of the stick were $\mu_\alpha = 1.5\,\mathrm{mm}^{-1}$ and $\mu_s' = 0.6\,\mathrm{mm}^{-1}$, respectively. For fluorescence measurements, a plastic tube filled with Rhodamine aqueous solutions was submerged in the same liquid phantom. The concentration of Rhodamine in the tube was 0.2 mg/ml.

The principle and characteristics of the LOT system have been given in Refs. 13, 16 and 18. Briefly, LOT technique utilizes instrumentation similar to a laser scanning confocal microscope and can acquire both diffused reflected light and fluorescence emission. However, LOT detects photons emerging from the medium at successive lateral distances from the beam's focus. The separation distance between the laser source and the detectors can be controlled by optical magnification of the system. The imaging depth can reach $\sim 2-3$ mm with spatial resolution around hundred microns.[13–16] Low numerical aperture (NA) objective lens was adopted in the LOT system to avoid measurement errors caused by surface unflatness. Therefore, the acceptance angle of the LOT system is small ($\sim 4.5$ degrees).

Figure 3 schematically shows the experimental setup. The LOT system scanned the focused laser beam within a square area (along $x$ and $y$ directions) on the top of the liquid phantom (without the absorbing stick) and simultaneously acquired signals for seven detectors with different separations from the light source. For each detector, a set of 2D data (along $x$- and $y$-axis) was obtained. These data were used as the background signals. Then, the vessel-like absorbing stick was submerged into the homogeneous resin solution along $y$-axis and parallel to the surface of the liquid phantom.

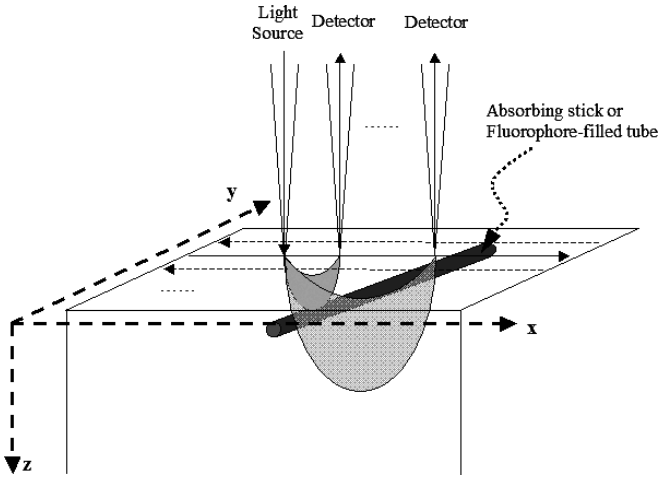


Fig. 3. A schematic drawing of the experimental setup.

For each stick depth, LOT scanned the same square area as before and simultaneously acquired data for the seven channels. These data were called heterogeneous data. Like the background signals, each channel acquired a set of 2D data (along $x$- and $y$-axis). For each channel, both the background signals and the heterogeneous data were averaged along $y$ direction, thus, the 2D data became 1D data (along $x$-axis). The averaged background signals were subtracted from the averaged heterogeneous data. To normalize the difference data, the 1D background data were further averaged (along $x$-axis) and became a number for each channel, and this number was used to normalize the difference data. The normalized difference was multiplied by 100 and converted into percentage of the perturbation. Consequently, each channel obtained a set of 1D data (along $x$-axis) about the percentage of the perturbation caused by the absorbing stick for each stick depth. Increasing the stick depth from 0.25 mm to 4 mm with an increment of 0.25 mm, repeating the above data acquiring and processing procedures, formatting all the data into a 3D structure ($z$, $x$, channel) in MATLAB (Mathworks, MA), displaying the data in $x-z$ plane for all channels, one can compare the experimentally measured relative perturbations with the theoretically estimated perturbations in $x-z$ plane for all channels.

Similar procedures were performed for the Rhodamine-filled tube, but there is no need for subtracting the background signals because there is no Rhodamine added in the homogeneous phantom. Therefore, the maximum value of the signal at a depth $z = 2$ mm was arbitrarily chosen as the normalization factor for each channel.

## 4. Results and Discussions

### 4.1. *Absorption perturbation*

Figure 4 displays the logarithm of the experimentally measured relative perturbations ($\log_{10} \cdot (\Delta M/M_0 \times 100)$) in $x-z$ plane for the seven detectors with different source–detector separations. Data shown in Fig. 4 have been interpolated based on the original experimental data using MATLAB. The source–detector separation distance is listed on the upper-right corner of each image, which is 0, 0.4, 0.6, 0.8, 1.2, 1.6, 2.0 mm, respectively. Color intensity represents the percentage of the perturbation. It is clear that the wider the source–detector separation is, the deeper the light can probe. Also, the closer the stick is to the source

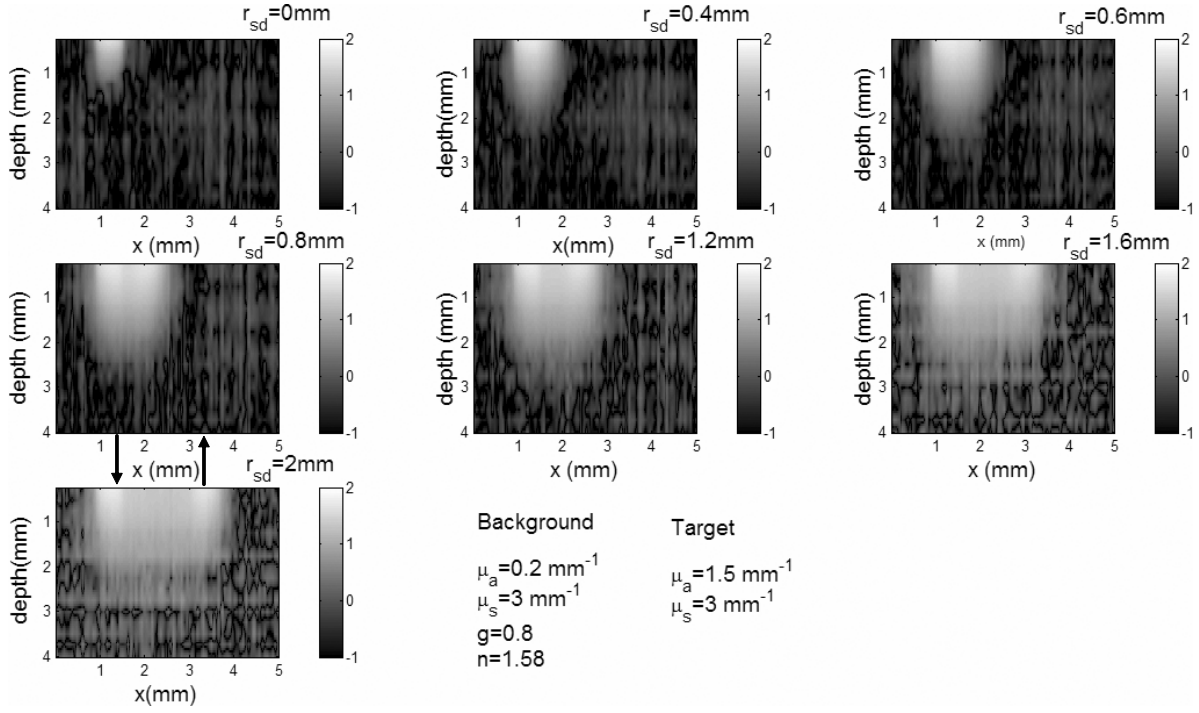


Fig. 4. Experimental data of the logarithm of the relative perturbation caused by an absorbing stick in $x-z$ plane for different source–detector separations. The separation distance is shown on the upper-right corner of each image. Optical parameters of the medium are listed on the figure and text. As an example, the arrows indicated on the last image represent the source and the detector positions.

or the detector, the larger the relative perturbation is. Limited by the system noise, the perturbation less than 0.1% cannot be detected.

To use delta-P1 approximation to calculate the relative perturbations, anisotropy factor $g$ is needed. By fitting MC-simulated data to these experimental data, it has been found that perturbation is much more sensitive to the absorption coefficient $\mu_a$ and the reduced scattering coefficient $\mu_s'$ than to the anisotropy factor $g$ when $g$ is between 0.6–0.9 for non-zero source–detector separation. Therefore, 0.8 is used as the estimated value for $g$ although it is larger than the measured value 0.5 at near infrared region in Ref. 32. It should be pointed out that similar results can be obtained no matter what value of $g$ is chosen between 0.9 to 0.6, as long as the same reduced scattering coefficient and absorption coefficient are used. Similar results have been reported in Refs. 34 and 35, which is attributed to the similarity relation.

Figure 5 shows the corresponding results calculated from delta-P1 approximation. Figure 5(a) displays the logarithm of the relative perturbation ($\log_{10}[(\exp(\Delta\Phi_i/\Phi_{0i}) - 1) \times 100]$) in $x-z$ plane. To compare Fig. 5(a) with Fig. 4, the contours at 3%, 15%, and 25% of two sets of data were plotted in Fig. 5(b). Solid lines represent the experimental data and dotted lines represent the simulated data from the delta-P1 approximation, respectively. The simulated data have large errors relative to the experimental data for short source–detector separations, such as $r_{sd} = 0$ and 0.4 mm. When $r_{sd}$ increases, the errors between two sets of data reduce, especially for small perturbations (3% and 15%). When the heterogeneity is close to the source or detectors (where large perturbations occur), large errors exist.

Figures 6(a) and 6(b) respectively represents the relative perturbation as a function of the stick depth for the experiment data and delta-P1 simulated data along a line directly underneath the light source (see the dotted line on the last image of Fig. 5(a)) and the middle line between the source and the detector (see the dashed line indicated on the last image of Fig. 5(a)). The arrows and numbers in Fig. 6 indicate the relative errors between the simulated perturbations and the experimentally measured perturbations at specific depths (note all errors were presented as positive to avoid cancellations when averaging the errors). Figure 6(a) shows that delta-P1 underestimates the relative perturbations for all channels when the depth is $< 0.5$ mm. Large errors between the simulated and experimental perturbations exist in this region (depth is $< 0.5$ mm) in both Figs. 6(a) and 6(b). Figure 6 implies that delta-P1 approximation generates large errors at the first two channels ($r_{sd} = 0$ and 0.4 mm). Therefore, the data acquired from these two channels may not be used for image reconstruction. When ignoring the data of the first two channels, the averaged errors of all other channels for depth = 0.25 mm in Figs. 6(a) and 6(b) are 39.45% and 39.81%, respectively (see Table 1). When depth is between 0.5 and 1.5 mm, the relative errors are reduced. For example, the averaged relative errors for depth = 1.0 mm of Figs. 6(a) and 6(b) are 13.93% and 13.88%, respectively. When depth $> 1.5$ mm, the relative errors rise again but are smaller than the errors in the shallow region (depth $< 0.5$ mm). For example, the averaged relative errors for depth = 2.0 mm of Figs. 6(a) and 6(b) are 24.86% and 30.97%, respectively. This may be partially caused due to the increase of the measurement errors. Table 1 summarizes the averaged relative errors.

Some singular points occur in Fig. 5(a). As an example, a white circle in the first image indicates a singular point. This is because the integration in Eq. (4) was performed by Gaussian quadrature with a Legendre polynomial weighting function.[22,36] In this method, the roots of the Legendre polynomial determine the $z$ positions of the point sources on the line source. When any roots happen to overlap with or are very close to any node of the grid, zero or very small distance between the point source and the note occur, which leads to large calculated fluence because the fluence is inversely related to the distance (see Eq. (4)). The sizes of the singular points in Fig. 5(a) reflect the stick diameter. Therefore, these singular points should be replaced by the average of the surrounding data points in the sensitivity matrix.

### 4.2. *Fluorescence perturbation*

Figure 7 shows the logarithm of the experimentally measured normalized fluorescence perturbations ($\log_{10}(M_{fl}(r_s, r_d)/M_{fl}(r_s, r_0) \times 100)$) in $x-z$ plane for different source–detector separations. As mentioned in Sec. 3, the normalization factor $M_{fl}(r_s, r_0)$ can be any point on each image (but better to use the data from the same location for all the channels). Compared with Fig. 4, Fig. 7 indicates that fluorescence perturbation is more diffused than

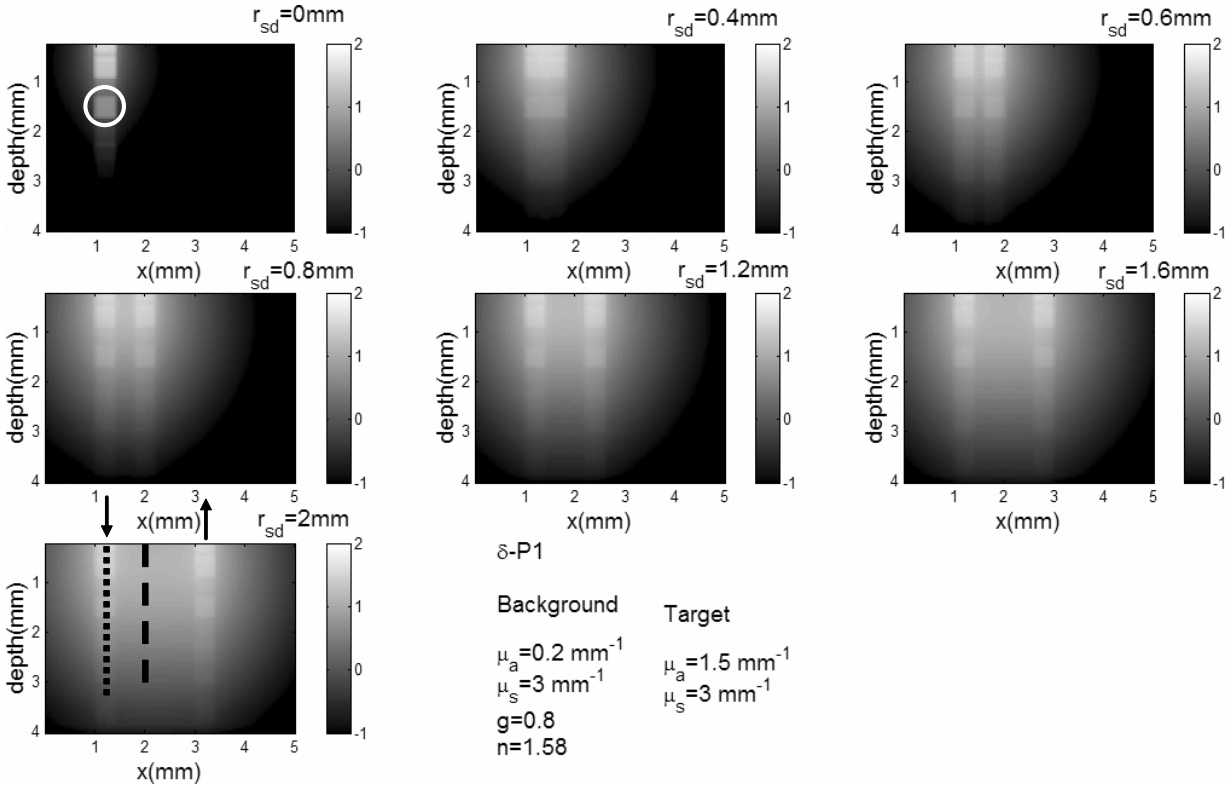


(a)

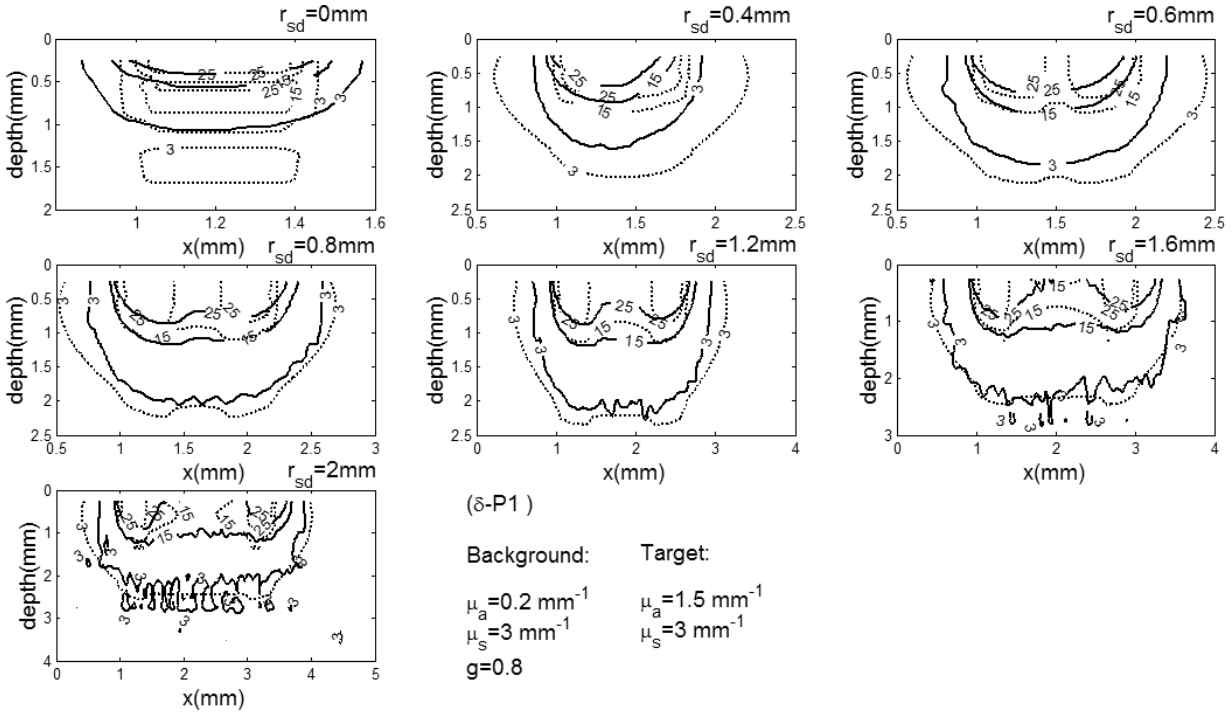


(b)

Fig. 5. (a) The logarithm of the relative perturbation in $x-z$ plane calculated based on the delta-P1 approximation. Background parameters were listed on the figure. (b) Contour distributions of (a) (3%, 15% and 25%). The solid and dotted lines represent the experimental data and the simulated data, respectively.

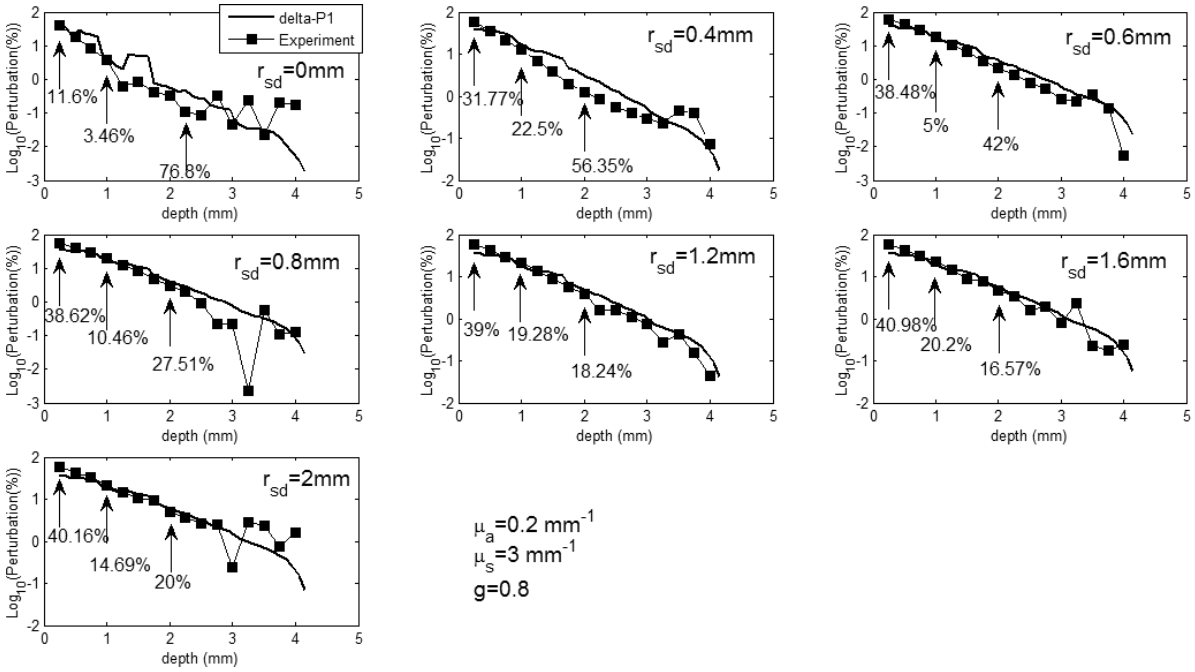


(a)

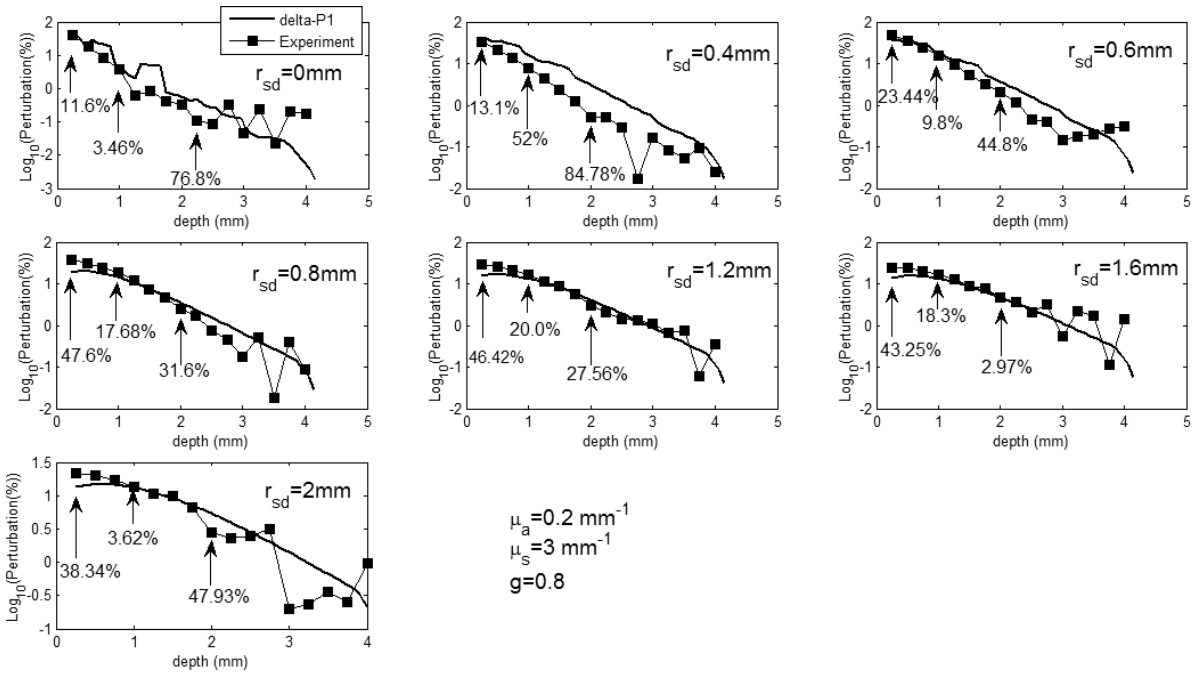


(b)

Fig. 6. (a) The logarithm of the relative perturbation as a function of the stick depth (along the line directly underneath the light source, such as the dotted line on the last image in Fig. 5(a), for all the source–detector separations). (b) Similar data but along the middle lines between the sources and the detectors for all separations, such as the dashed line on the last image in Fig. 5(a).

absorption perturbation. This is reasonable because the emission of fluorescence is isotropic. Therefore, the delta-P1 approximation is expected to provide more accurate estimation for fluorescence perturbations. This is verified by Figs. 8 and 9. Figure 8(a) shows the logarithm of the normalized fluorescence perturbation calculated from delta-P1 approximation. Since the differences of both the absorption

Table 1. Averaged errors of delta-P1 simulated perturbations relative to the experimentally measured perturbations. The data samples were taken from Figs. 6 and 9.

| | Relative errors of absorption perturbation | | | Relative errors of fluorescent perturbation | | |
|---|---|---|---|---|---|---|
| | $D = 0.25$ mm | $D = 1.0$ mm | $D = 2.0$ mm | $D = 0.25$ mm | $D = 1.5$ mm | $D = 3.0$ mm |
| Line 1 | 39.45% (W) (± 1.08%) | 13.93% (W) (± 6.33%) | 24.86% (W) (± 10.45%) | **53.63%** (± 14.3%) | 13.45% (± 13.77%) | 22.16% (± 18.39%) |
| | | | | **47.32%** (W) (± 10.93%) | 7.45% (W) (± 4.2%) | 15.79% (W) (± 13.13%) |
| Middle line | 39.81% (W) (± 9.83%) | 13.88% (W) (± 6.95%) | 30.97% (W) (± 17.85%) | 23.63% (± 27.54%) | 13.42% (± 14.26%) | 25.18% (± 18.51%) |
| | | | | 8.37% (W) (± 6.2%) | 7.1% (W) (± 5.63%) | 17.49% (W) (± 13.78%) |

*Note*: For a specific depth, the relative errors from all the channels or the last five channels (indicated as W) were averaged and indicated in the table. The data in parentheses in the table showed the standard deviations. $D$: depth of the stick or the fluorophore-filled tube; (W): without considering the first two channels ($r_{sd} = 0$ and 0.4 mm); Line 1: the line underneath the light source; Middle line: the middle line between a source and a detector.

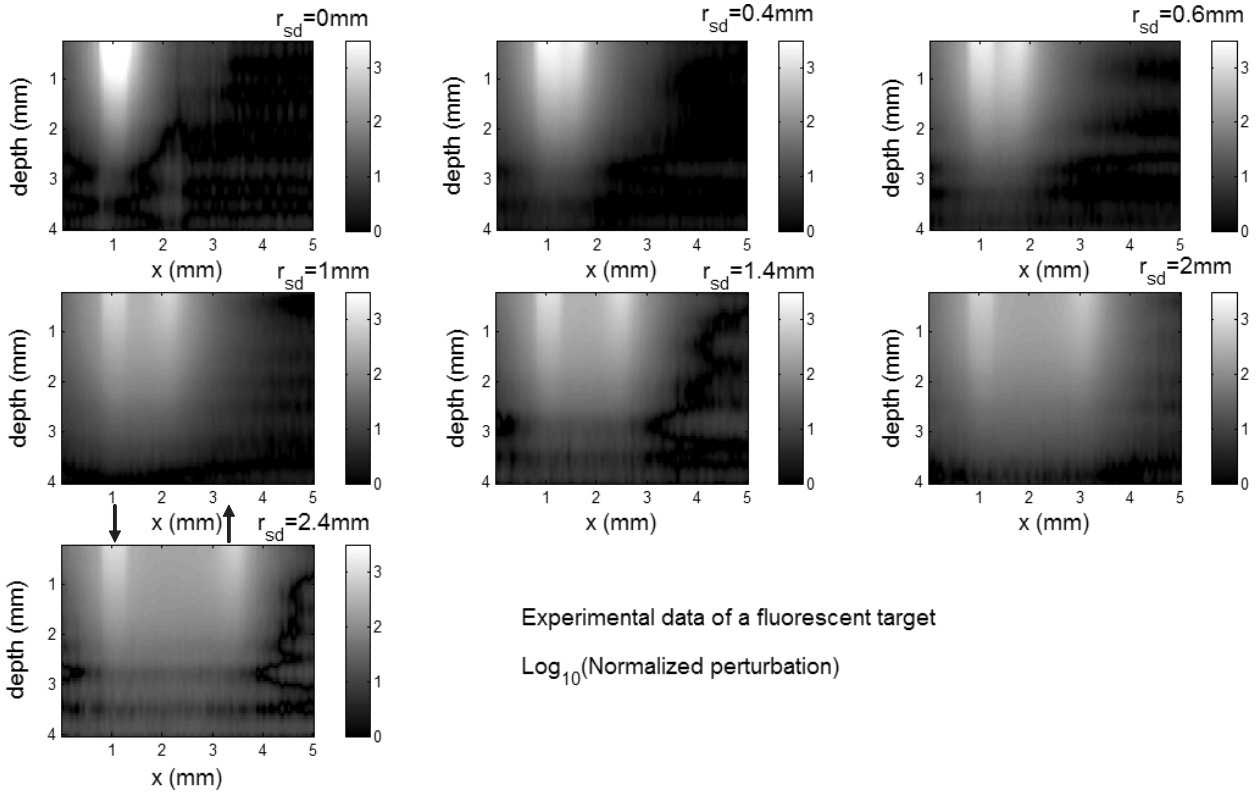


Fig. 7. Experimental data of the logarithm of the normalized fluorescence perturbation caused by the Rhodamine-filled tube in $x-z$ plane for different source–detector separations. The separation distance is shown on the upper-right corner of each image. Optical parameters of the background medium are same as those shown in Fig. 4. As an example, the arrows indicated on the last image represent the source and the detector positions.

coefficient and the scattering coefficient between the excitation light and the emission light are ignored, essentially Fig. 8(a) was calculated based on the same formulas and same parameters as those used for Fig. 5(a) except the normalization factor. Similar contours (5%, 90%, and 300%) are plotted in Fig. 8(b). The numbers marked on the contours are relative to the normalization factor. In Fig. 8(b), all

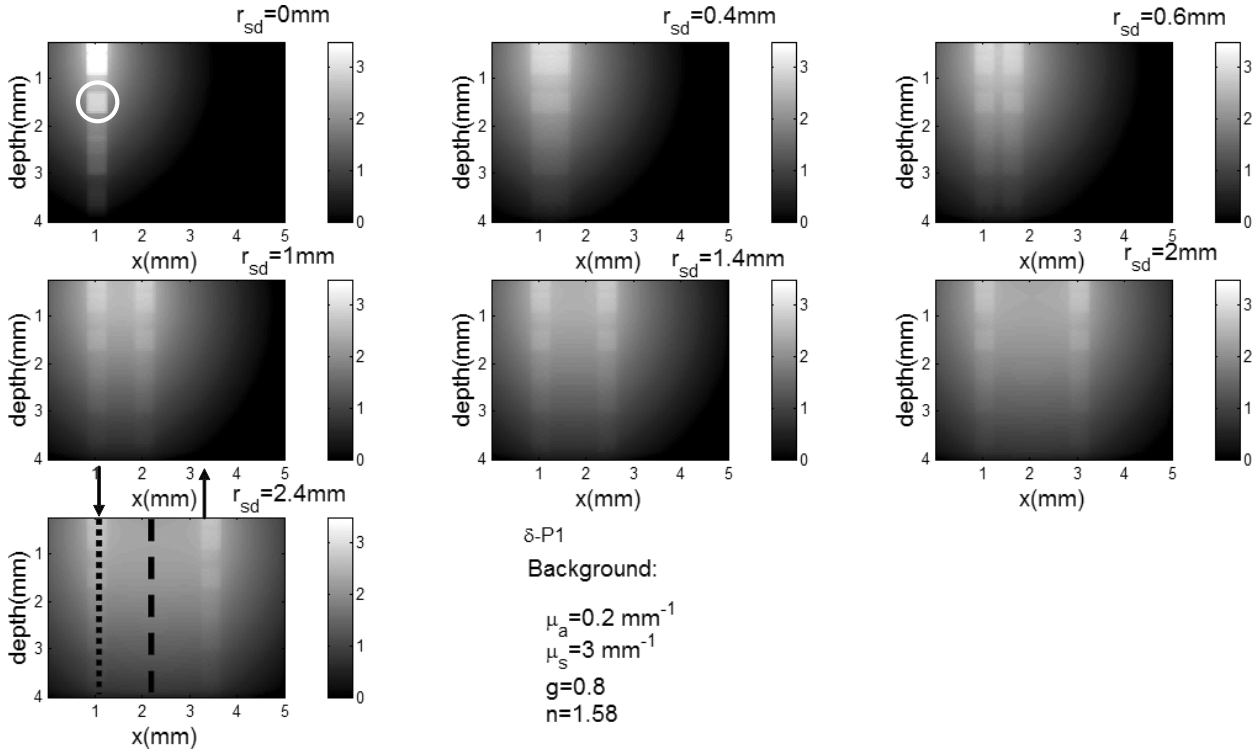


(a)

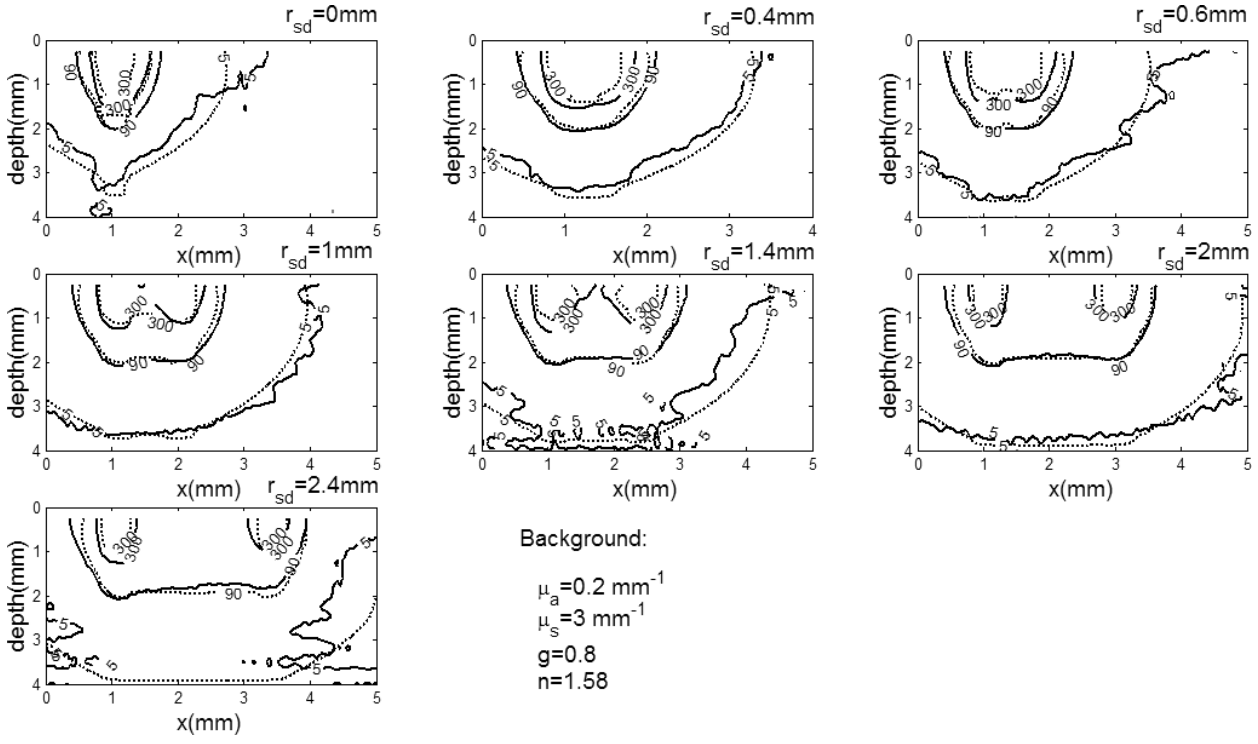


(b)

Fig. 8. (a) The logarithm of the normalized fluorescence perturbation in $x-z$ plane calculated based on the delta-P1 approximation. (b) Contour distributions of (a) (5%, 90% and 300%). The solid and dotted lines represent the experimental data and the simulated data, respectively. All the parameters of the background medium are the same as those in Fig. 5.

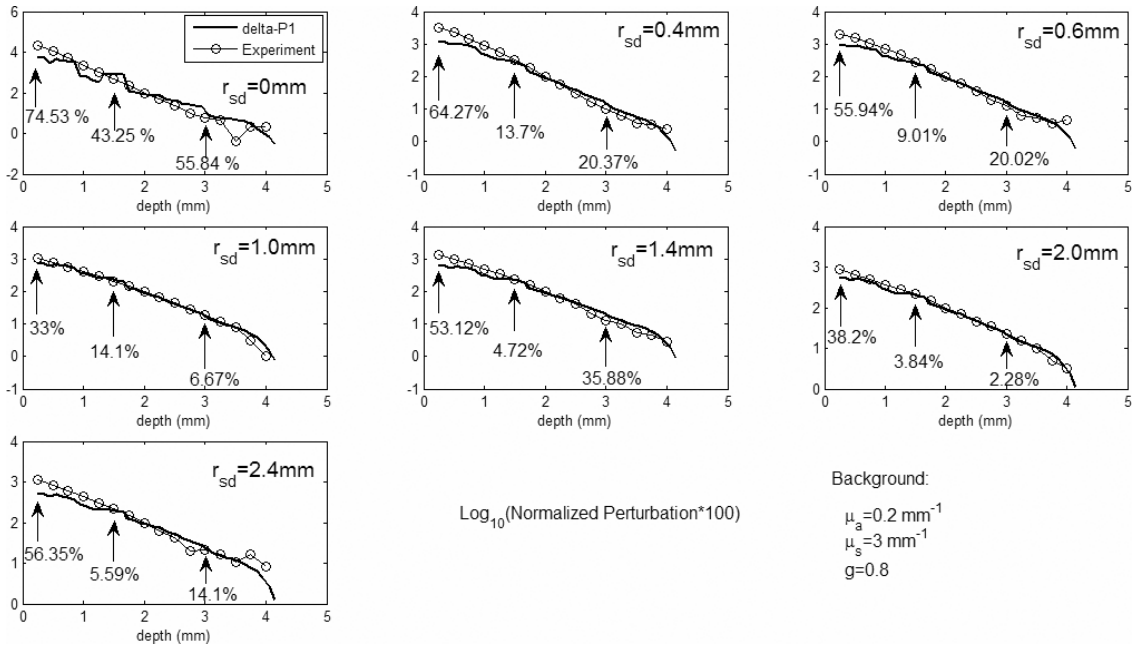


(a)

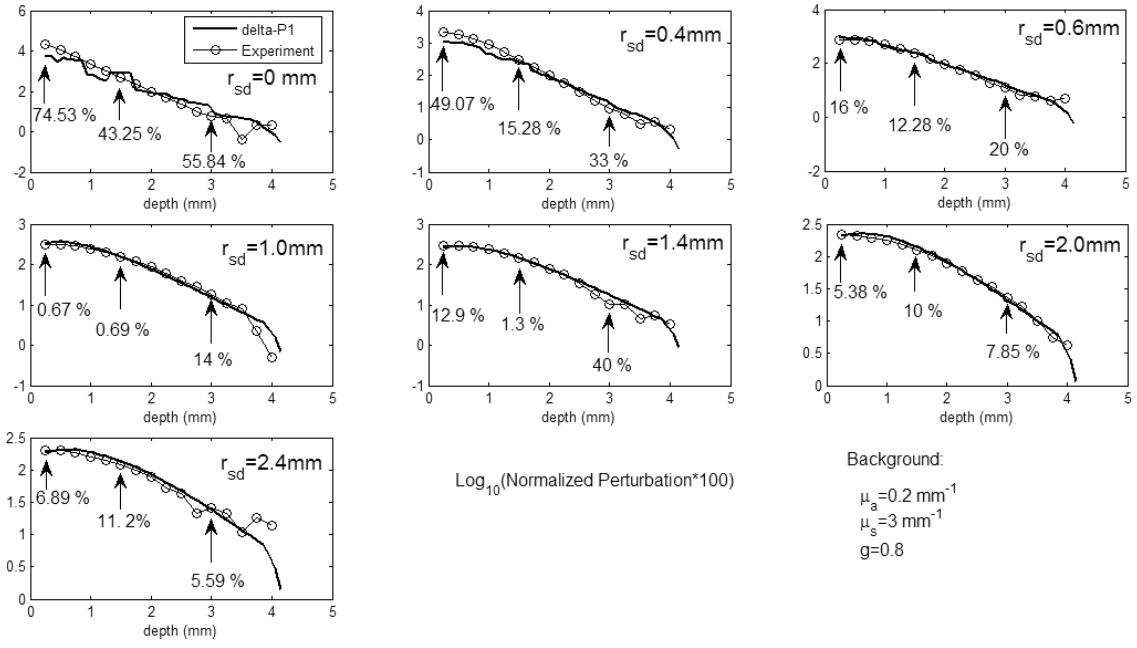


(b)

Fig. 9. (a) The logarithm of the normalized fluorescence perturbation as a function of the tube depth along the line directly underneath the light source, such as the dotted line on the last image in Fig. 8(a), for all the source–detector separations. (b) Similar data but along the middle lines between the sources and the detectors for all separations, such as the dotted line on the last image in Fig. 8(a).

channels show good agreements between the experimental data (solid lines) and the delta-P1 simulated data (dotted lines).

Similar to Figs. 6(a) and 6(b), Figs. 9(a) and 9(b) plot the normalized fluorescence perturbation as a function of the depth of the fluorescent tube for the experiment data and the simulated data along the line directly underneath the light source and the middle line between the source and detectors, respectively. The relative errors at depth = 0.25, 1.5, and 3.0 mm were indicated in the figure. The averaged relative errors of the different

channels at the three depths are provided in Table 1. The data marked with "W" mean that these data were calculated without considering the first two channels. Comparing these data with those of absorption perturbations, one can find that the averaged relative errors of fluorescence perturbations reduce obviously for both shallow and depth regions (7.45% and 7.1% when depth = 1.5 mm, and 15.79% and 17.49% when depth = 3.0 mm). The exceptions are the location very close to the light source, 0.25 mm underneath the light source where the averaged relative error reaches 47.32%, and the location very close to the detector (data not shown). This result may be caused by the intrinsic limitations of the diffusion model. Since the signal-to-noise ratio in the measurements degraded, the averaged relative errors increased when the depth was increased from 1.5 to 3 mm. When the first two channels were included, the averaged relative errors increased. Unlike other studies[21,22] in which the errors of *fluences* between the simulated and experimental data were discussed, the data in Table 1 and the numbers associated with the arrows in Figs. 6 and 9 are errors between the predicted and experimentally measured signal *perturbations* that were generated by the heterogeneities. Therefore, averaged errors less than 40% for the absorption perturbations (without considering the first two channels) may still be acceptable for some LOT applications in which the reconstruction speed is more interesting or preliminary image reconstruction is wanted before adopting more sophisticated methods, such as MC simulations. For fluorescence perturbations, delta-P1 provided less than 20% averaged errors (without considering the first two channels and the locations close to the source and the detectors) and therefore it should be an appropriate approximation for the applications of fluorescence LOT.

### 4.3. *Possible error sources*

Possible reasons causing the errors between the experimental data and the delta-P1 approximation can be summarized as follows. Firstly, in present study, the fluence is assumed to be proportional to the LOT signals. However, for very short source–detector separations as shown in Fig. (2), the ratio diverges from the constant (indicated by the black line). The distance ($l$) at which the ratio starts diverging from the constant is related to the transport albedo. Figure 10 plots MC simulated data for $l$ as a function of absorption coefficient ($\mu_a$)

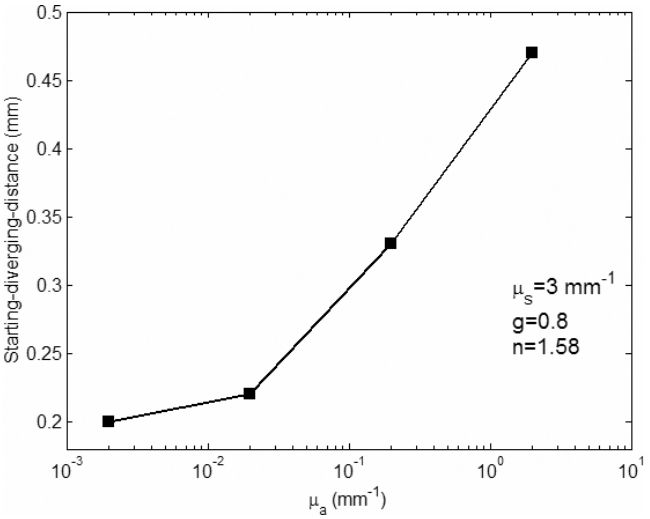


Fig. 10. The starting-diverging-distance $l$ indicated in Fig. 2 as a function of the medium absorption coefficient. $X$-axis is in log scale.

while the reduced scattering coefficient ($\mu_s'$) is maintained as a constant (0.6 mm$^{-1}$). The corresponding transport albedo along $x$-axis is 0.997, 0.968, 0.750, and 0.231. When the source–detector separation is less than $l$, radiance, instead of the fluence, should be used for calculating LOT signals. This result explains the fact that large errors always occur for short source–detector separations. Based on the results shown in Fig. 10, it is reasonable to believe that the delta-P1 approximation should provide more accurate estimations than those shown in Figs. (5) and (6) and Figs. (8) and (9) when increasing the transport albedo. This was verified by comparing the results calculated from delta-P1 approximation with those calculated from MC simulation for albedo of 0.97 and 0.99 (data not shown). Secondly, although the delta-Eddington phase function and the line source incorporated in delta-P1 approximation can release the pressure on diffusion approximation to a certain degree, delta-P1 approximation still produces certain errors in the region surrounding the light source and detectors[21–24] because of the intrinsic limitations of diffusion models. Thirdly, the Rytov approximation and the reciprocity approximation can also generate errors in the calculations of perturbations. In addition, noises in LOT measurements may lead to certain errors, especially for deep regions.

## 5. Summary and Conclusions

The relative errors of perturbations between the delta-P1-simulated and experimentally measured

data were quantified. For absorption perturbations, large relative errors were found when source–detector separations were very small (such as $r_{sd} = 0$ and 0.4 mm) or when the heterogeneity was very close to the source or detectors. However, for large source–detector separations and deep heterogeneities, the channel-averaged relative errors of perturbations were found to be less than 40%, which implies that delta-P1 approximation may be used as a forward model for rapid image reconstruction before adopting more sophisticated methods, such as MC simulations. The relative errors of fluorescence perturbations were found to be much smaller than those of absorption perturbations because of the isotropic property of the emission light, which implies that delta-P1 approximation is a good model for rapid image reconstruction in fluorescence LOT. The model's accuracy can be further improved when used for a medium with higher transport albedo.

## Acknowledgments

I acknowledge the start-up funding support from The Catholic University of America and Dr Elizabeth M. C. Hillman's instructions in the experiments.

## Appendix A

As pointed out by Haskell[25] and Hull,[35] the measured signal by an optical fiber placed at the surface or a lens on the top of a semi-infinite medium can be expressed as

$$\begin{aligned}\text{Signal}(\rho, z=0) &= \iint_A dA \int_0^{2\pi} d\varphi \int_0^{\theta_0} \sin\theta d\theta \\ &\quad \cdot R_d(x, y, z=0, \hat{s})(\hat{s}\cdot\hat{n}) \\ &\approx 2\pi A \int_0^{\theta_0} \sin\theta\cos\theta\, R_d(x, y, 0, \theta) d\theta, \end{aligned} \tag{A1}$$

where $A$ is the detector area, $\theta_0$ is the acceptance angle of the measurement system, $R_d(x, y, z=0, \hat{s})$ is the diffused reflectance at the position of $(x, y, z = 0)$ and the direction of $\hat{s}$. The area is assumed so small that the $R_d(x, y, z=0, \hat{s})$ is considered independent of spatial position within the area $A$. Equation (A1) implies that the measured signal is proportional to the angular integral of the diffused reflectance at the medium surface.

## Appendix B

The relative perturbation caused by an absorbing target can be expressed as[5–9,37]

$$\frac{\Delta\Phi(r_{si}, r_{di})}{\Phi_0(r_{si}, r_{di})} = \frac{-\int_\Omega \Phi_0(r_{si}, r) G(r, r_{di}) \Delta\mu_a(r) dr^3}{\Phi_0(r_{si}, r_{di})}. \tag{B1}$$

$\Delta\Phi(r_{si}, r_{di})$ is the fluence perturbation measured at the $i$th source–detector pair with and without the absorbing target, $\Phi_0(r_{si}, r_{di})$ represents the fluence at the position of the $i$th detector generated by the $i$th source, $\Phi_0(r_{si}, r)$ is the fluence at position $r$ generated by the $i$th source with unit of Watts/mm$^2$, $G(r, r_{di})$ represents the Green's function and represents a photon propagation factor from the position $r$ to the position of the $i$th detector $(r_{di})$, which has a unit of mm$^{-2}$ if diffusion coefficient $D$ is included, $\Delta\mu_a(r)$ is the perturbation of absorption coefficient at position $r$, and $\Omega$ is the target volume. Digitizing the integral in Eq. (B1), the following approximation is given

$$\begin{aligned}\frac{\Delta\Phi(r_{si}, r_{di})}{\Phi_0(r_{si}, r_{di})} &\approx \frac{-\sum_{j=1}^{N} \Delta v \cdot \Phi_0(r_{si}, r_j) \cdot G(r_j, r_{di}) \cdot \Delta\mu_a(r_j)}{\Phi_0(r_{si}, r_{di})} \\ &= \frac{-\sum_{j=1}^{N} \Delta v \cdot \Phi_0(r_{si}, r_j) \cdot \Phi_0(r_{si}, |\mathbf{r}_j - \mathbf{r}_{di}|) \Delta\mu_a(r_j)}{\Phi_0(r_{si}, r_{di}) S_0}. \end{aligned} \tag{B2}$$

In the second line, $\Phi_0(r_{si}, |\mathbf{r}_j - \mathbf{r}_{di}|)/S_0$ is used to replace the Green's function in the first line. $S_0$ is a constant with unit of Watts. Figure B1 shows the fluence distributions in $x-z$ plane calculated from MC simulation, and the principle of reciprocity is indicated. By setting $\mathbf{r}_{si} = 0$ and $R$ denoting an arbitrary voxel, the relative fluence perturbation caused by $\Delta\mu_a$ at position $R$ is expressed as Eq. (B2) in which $\Phi_0(r_{si}, r_j)$ and $G(r_j, r_{di})$ are a function of $|\mathbf{r}_j|$ and $|\mathbf{r}_{di} - \mathbf{r}_j|$, respectively. Reciprocity states that the probability of a photon propagating from the point $S$ to the point $R$ is assumed to be equal to the probability of the photon propagating from the point $R$ to the point $S$.[26] If the source is assumed to be completely equivalent to the detector, photon propagation from point $R$ to point $D$ is equivalent to from $R'$ to $S$, and therefore is equivalent to from

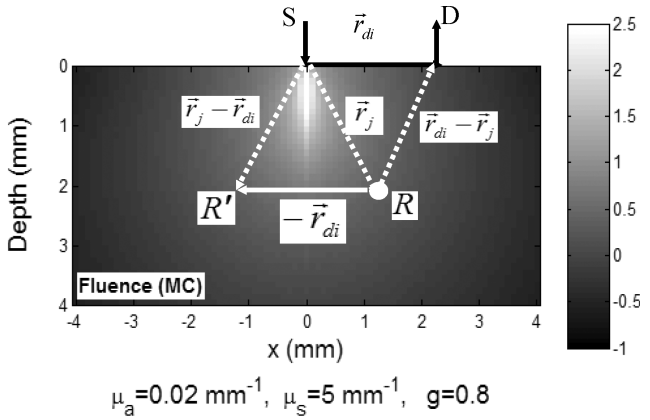


Fig. B1. A schematic drawing shows the principle of the approximation of the reciprocity. Fluence distribution in $x-z$ plane was calculated from MC simulation.

$S$ to $R'$. Consequently, the unknown Green's function, $G(r_j, r_{di})$, which represents the propagation factor from point $R$ to point $D$, can be replaced with the fluence at $R'$ divided by a power constant $S_0$ (which is represented as $\Phi_0(r_{si}, |\mathbf{r}_j - \mathbf{r}_{di}|)/S_0$). To make the sensitivity matrices nondimensional, the fluence ($\Phi_0(r_{si}, r_0)$) at any position $r_0$ generated by the $i$th source is used as a normalization factor:

$$\begin{aligned}
&\frac{\Delta\Phi(r_{si}, r_{di})}{\Phi_0(r_{si}, r_{di})} \\
&\quad\approx \frac{-\sum_{i=1}^{N} \Delta v \cdot \left(\frac{\Phi_0(r_{si}, r_j)}{\Phi_0(r_{si}, r_0)}\right) \cdot \left(\frac{\Phi_0(r_{si}, \mathbf{r}_j - \mathbf{r}_{di})}{\Phi_0(r_{si}, r_0)}\right)}{\left(\frac{\Phi_0(r_{si}, r_{di})}{\Phi_0(r_{si}, r_0)}\right)} \\
&\qquad \cdot \left(\frac{\Phi_0(r_{si}, r_0)}{S_0}\right) \Delta\mu_a(r_j) \\
&\quad = W_{ij}(r_{si}, r_j, r_{di}) \left(\frac{\Phi_0(r_{si}, r_0)}{S_0} \Delta\mu_a(r_j)\right),
\end{aligned} \tag{B3}$$

where $W_{ij}(r_{si}, r_j, r_{di})$ is defined by Eq. (8).

## References


1. Star, W. M., in *Optical-Thermal Response of Laser-Irradiated Tissue*, eds. Welch, A. J. and van Gemert, M. J. C. (Plenum, New York, 1995), 131–206.
2. Murphy, B., *Fundamentals of Light Microscopy and Electronic Imaging* (Wiley-Liss, 2001).
3. Yodh, A. and Chance, B., "Spectroscopy and imaging with diffusing light," *Phys. Today* **3**, 34–40 (1995).
4. Tromberg, B. J., Shah, R., Lanning, A., Cerussi, J., Espinoza, T., Pham, L., Svaasand, L. and Butler, J., "Noninvasive *in vivo* characterization of breast tumors using photon migration spectroscopy," *Neoplasia* **2**, 26–40 (2000).
5. Milstein, A. B., Oh, S., Webb, K. J., Bouman, C. A., Zhang, Q., Boas, D. A. and Millane, R. P., "Fluorescence optical diffusion tomography," *Appl. Opt.* **42**, 3081–3094 (2003).
6. O'Leary, M. A., Boas, D. A., Chance, B. and Yodh, A. G., "Experimental images of heterogeneous turbid media by frequency-domain diffusing-photon tomography," *Opt. Lett.* **20**, 426–428 (1995).
7. O'Leary, M. A., Boas, D. A., Li, X. D., Chance, B. and Yodh, A. G., "Fluorescence lifetime imaging in turbid media," *Opt. Lett.* **21**, 158–160 (1996).
8. Ntziachristos, V. and Weissleder, R., "Experimental three-dimensional fluorescence reconstruction of diffuse media by use of a normalized Born approximation," *Opt. Lett.* **26**, 893–895 (2001).
9. Gurfinkel, M., Ke, S., Wen, X., Li, C. and Sevick-Muraca, E. M., "Near-infrared fluorescence optical imaging and tomography," *Dis. Markers* **19**, 107–121 (2003, 2004).
10. Seo, I., You, J. S., Hayakawa, C. K. and Venugopalan, V., "Perturbation and differential Monte Carlo methods for measurement of optical properties in a layered epithelial tissue model," *J. Biomed. Opt.* **12**, 014030 (2007).
11. Bevilacqua, F. and Depeursinge, C., "Monte Carlo study of diffuse reflectance at source-detector separations close to one transport mean free path," *J. Opt. Soc. Am. A* **16**, 2935–2945 (1999).
12. Klose, A. D. and Hielscher, A. H., "Fluorescence tomography with simulated data based on the equation of radiative transfer," *Opt. Lett.* **28**, 1019–1021 (2003).
13. Hillman, E. M. C., Boas, D. A., Dale, A. M. and Dunn, A. K., "Laminar Optical Tomography: Demonstration of millimeter-scale depth-resolved imaging in turbid media," *Opt. Lett.* **29**, 1650–1652 (2004).
14. Hillman, E. M. C., Devor, A., Bouchard, M. B., Dunn, A. K., Krauss, G. W., Skoch, J., Bacskai, J., Dale, A. M. and Boas, D. A., "Depth-resolved optical imaging and microscopy of vascular compartment dynamics during somatosensory stimulation," *Neuroimage* **35**, 89–104 (2007).
15. Hillman, E. M. C., Bernus, O., Pease, E., Bouchard, M. B. and Pertsov, A., "Depth-resolved optical imaging of transmural electrical propagation in perfused heart," *Opt. Express* **15**, 17827–17841 (2007).
16. Burgess, S. A., Bouchard, M. B., Yuan, B. and Hillman, E. M. C., "Simultaneous multi-wavelength laminar optical tomography," *Opt. Lett.* **33**, 2710–2712 (2008).

17. Yuan, B., Burgess, S. A., Bouchard, M. B., Lehrer, N., Iranmahboob, A. and Hillman, E. M. C., "A system for high-resolution depth-resolved optical imaging of fluorescence and absorption contrast," (accepted by *Review of Scientific Instruments*).
18. Burgess, S. A., Yuan, B., Bouchard, M. B., Ratner, D. and Hillman, E. M. C., "Simultaneous multiwavelength laminar optical tomography imaging of skin cancer," *OSA BIOMED FL* (March 2008).
19. Star, W. M., *Dosimetry of Laser Radiation in Medicine and Biology,* eds. Müller, G. J. and Sliney, D. H. (SPIE, Bellingham, WA), 146–154 (1989).
20. Prahl, S. A., "Light transport in tissue," PhD dissertation, University of Texas at Austin (1988).
21. Venugopalan, V., You, J. S. and Tromberg, B. J., "Radiative transport in the diffusion approximation: An extension for highly absorbing media and small source–detector separations," *Phys. Rev. E* **58**, 2395–2407 (1998).
22. Seo, I., Hayakawa, C. K. and Venugopalan, V., "Radiative transport in the delta-P1 approximation for semi-infinite turbid media," *Med. Phys.* **35**, 681–693 (2008).
23. You, J. S., Hayakawa, C. K. and Venugopalan, V., "Frequency domain photon migration in the delta-P1 approximation: Analysis of ballistic, transport, and diffuse regimes," *Phys. Rev. E* **72**, 021903-1-13 (2005).
24. Carp, S. A., Prahl, S. A. and Venugopalan, V., "Radiative transport in the delta-P1 approximation: Accuracy of fluence rate and optical penetration depth predictions in turbid semi-infinite media," *J. Biomed. Opt.* **9**, 632–647 (2004).
25. Haskell, R. C., Svaasand, L. O., Tsay, T., Feng, T., McAdams, M. S. and Tromberg, B. J., "Boundary conditions for the diffusion equation in radiative transfer," *J. Opt. Soc. Am. A* **10**, 2727–2741 (1994).
26. Ma, G., Delorme, G. F., Gallant, P. and Boas, D. A., "Comparison of simplified Monte Carlo simulation and diffusion approximation for the fluorescence signal from phantoms with typical mouse tissue optical properties," *Appl. Opt.* **46**, 1686–1692 (2007).
27. Arridge, S. R. and Schweiger, M., "Photon-measurement density functions Part 2: Finite-element-method calculations," *Appl. Opt.* **34**, 8026–8037 (1995).
28. Dehghani, H., Davis, S. C. and Pogue, B. W., "Spectrally resolved bioluminescence tomography using the reciprocity approach," *Med. Phys.* **35**, 4863–4871 (2008).
29. Boas, D., Culver, J., Stott, J. and Dunn, A., "Three-dimensional Monte Carlo code for photon migration through complex heterogeneous media including the adult human head," *Opt. Express* **10**, 159–170 (2002).
30. Wang, L. H., Jacques, S. L. and Zheng, L. Q., "MCML — Monte Carlo modeling of photon transport in multi-layered tissues," *Comput. Meth. Prog. Biomed.* **47**, 131–146 (1995).
31. Wang, L. H., Jacques, S. L. and Zheng, L. Q., "CONV — Convolution for responses to a finite diameter photon beam incident on multi-layered tissues," *Comput. Meth. Prog. Biomed.* **54**, 141–150 (1997).
32. Firbank, M. and Delpy, D. T., "A design for a stable and reproducible phantom for use in near-infrared imaging and spectroscopy," *Phys. Med. Biol.* **38**, 847–853 (1993).
33. http://www.medphys.ucl.ac.uk/research/borl/research/NIR_topics/phantom_recipe.htm
34. Spott, T. and Svaasand, L. O., "Collimated light sources in the diffusion approximation," *Appl. Opt.* **39**, 6453–6465 (2000).
35. Hull, E. L. and Foster, T. H., "Steady-state reflectance spectroscopy in the P3 approximation," *J. Opt. Soc. Am. A* **18**, 584–599 (2001).
36. http://pathfinder.scar.utoronto.ca/∼dyer/csca57/book_P/node44.html
37. Yuan, B. and Zhu, Q., "Separately reconstructing the structural and functional parameters of a fluorescent inclusion embedded in a turbid medium," *Opt. Express* **14**, 7172–7187 (2006).